Machine learning filters out efficient electrocatalysts in the massive ternary alloy space for fuel cells

Youngtae Park [a,b,1], Chang-Kyu Hwang [c,d,1], Kihoon Bang [e], Doosun Hong [e], Hyobin Nam [c], Soonho Kwon [f], Byung Chul Yeo [g], Dohyun Go [h], Jihwan An [i], Byeong-Kwon Ju [d], Sang Hoon Kim [j], Ji Young Byun [j], Seung Yong Lee [c], Jong Min Kim [c,k,*], Donghun Kim [e,**], Sang Soo Han [e,**], Hyuck Mo Lee [a,**]

[a] *Department of Materials Science and Engineering, Korea Advanced Institute of Science and Technology (KAIST), 291 Daehak-ro, Yuseong-gu, Daejeon 34141, Republic of Korea*
[b] *Hydrogen Research Department, Korea Institute of Energy Research, 152 Gajeong-ro, Yuseong-gu, Daejeon 34129, Republic of Korea*
[c] *Materials Architecturing Research Center, Korea Institute of Science and Technology (KIST), 5 Hwarang-ro 14-gil, Seongbuk-gu, Seoul 02792, Republic of Korea*
[d] *Department of Micro/Nano System, Korea University, 145 Anam-ro, Seongbuk-gu, Seoul 02841, Republic of Korea*
[e] *Computational Science Research Center, Korea Institute of Science and Technology (KIST), 5 Hwarang-ro 14-gil, Seongbuk-gu, Seoul 02792, Republic of Korea*
[f] *Materials and Process Simulation Center (MSC), California Institute of Technology, Pasadena, CA, USA*
[g] *Department of Energy Resources Engineering, Pukyong National University, Busan 48513, Republic of Korea*
[h] *Department of Nano-bio Engineering Seoul National University of Science and Technology (SeoulTech), Gongneung-ro 232, Nowon-gu, Seoul 01811, Republic of Korea*
[i] *Department of Mechanical Engineering, Pohang University of Science and Technology (POSTECH), Cheongam-ro 77, Nam-gu, Pohang-si, Gyeongsangbuk-do 37673, Republic of Korea*
[j] *Extreme Materials Research Center, Korea Institute of Science and Technology (KIST), 5 Hwarang-ro 14-gil, Seongbuk-gu, Seoul 02792, Republic of Korea*
[k] *KHU-KIST Department of Converging Science and Technology, Kyung Hee University, Seoul 02447, Republic of Korea*

ARTICLE INFO

ABSTRACT

Despite their potential promise, multicomponent materials have not been actively considered as catalyst materials to date, mainly due to the massive compositional space. Here, targeting ternary electrocatalysts for fuel cells, we present a machine learning (ML)-driven catalyst screening protocol with the criteria of structural stability, catalytic performance, and cost-effectiveness. This process filters out only 10 and 37 candidates out of over three thousand test materials in the alloy core@shell ($X_3Y@Z$) for each cathode and anode of fuel cells. These candidates are potentially synthesizable, lower-cost and higher-performance than conventional Pt. A thin film of $Cu_3Au@Pt$, one of the final candidates for oxygen reduction reactions, was experimentally fabricated, which indeed outperformed a Pt film as confirmed by the approximately 2-fold increase in kinetic current density with the 2.7-fold reduction in the Pt usage. This demonstration supports that our ML-driven design strategy would be useful for exploring general multicomponent systems and catalysis problems.

1. Introduction

Platinum (Pt), a highly scarce and expensive element, is used as an indispensable ingredient in fuel cells. For the last decade, extensive efforts have been made to develop less expensive catalysts that maintain catalytic activities comparable to that of Pt [1–4]; however, the outcomes are still either pure Pt or merely a Pt-based modification [5–9].

For the cathode where the oxygen reduction reaction (ORR) should occur, Pt_3Ni (with Pt skin) is the state of the art; on the other hand, for the anode where the hydrogen oxidation reaction (HOR) should occur, unary Pt is used owing to its high activity despite the severe CO poisoning issue not being resolved [10]. It is highly desirable to find novel and lower-cost materials for both the cathode and anode without sacrificing the catalytic performance.

---

* Corresponding author at: Materials Architecturing Research Center, Korea Institute of Science and Technology (KIST), 5 Hwarang-ro 14-gil, Seongbuk-gu, Seoul 02792, Republic of Korea.
** Corresponding authors.
E-mail addresses: jongminkim@kist.re.kr (J.M. Kim), donghun@kist.re.kr (D. Kim), sangsoo@kist.re.kr (S.S. Han), hmlee@kaist.ac.kr (H.M. Lee).
[1] These authors contributed equally.

Metal alloying has been an excellent catalyst design strategy [11] since the alloying process can substantially modify the electronic structure and consequently the catalytic properties of metals. Alloying attempts in fuel cells thus far, however, have been limited to Pt-based bimetallic cases. In working environments, transition metals often dissolve while platinum does not, resulting in the formation of a Pt-based binary alloy with a Pt skin (Pt$_a$$X$$_b$@Pt, where X=arbitrary metal element) in the cathode of fuel cells. This Pt$_a$$X$$_b$@Pt structure has been extensively explored, and X ranges from (post-)transition metals (X=Ni, Co, Fe, Ti and Pb) [12,13] to other transition metals that are chemically similar to lanthanides (X=Y and Sc) [14]. These alloy nanostructures have exhibited improved performance because the Pt shell ensures stability in harsh environments and the alloy core offers tunability of the catalytic properties via ligand and geometric effects. In particular, Pt-Ni- [15], Pt-Co- [16,17], and Pt-Pb-based nanostructures in the cathode boost the mass activities (RDE test) into the range of 3.0–4.3 A/mg$_{Pt}$, which is considerably larger than the value of 0.1 A/mg$_{Pt}$ for pure Pt [16]. The enhancements in the activity were also supported by density functional theory (DFT) studies in which the overpotential values were computed to be as low as 0.4 V for Pt$_3$Ni or Pt$_3$Co, compared to 0.67 V for pure Pt.

Despite these achievements, Pt-based binary alloys have not been able to fully solve the chronic problems in fuel cells, which include high cost (dominance of the expensive Pt), slow kinetics (insufficient ORR activities at the cathode), and CO poisoning (a durability issue at the anode). These remaining problems call for the exploration of even broader compositional space, namely, ternary alloys [18–22]. In fact, the study of ternary space toward efficient ORR catalysis, including the examples of the Pt-Pd-Au [23] and Pt-Ni-Co [24,25] combinations, has only recently begun. This approach is a promising direction but is considered extremely difficult to explore due to the massive candidate space. For example, exploring ternary metal alloy materials involves numerous candidates. With only 30 metal elements, at least $_{30}C_3 = 4060$ elemental combinations exist, and adding the variation in crystal symmetry and elemental compositions results in an infinite number of material candidates. Such a massive space cannot be explored by trial-and-error experiments or expensive quantum mechanical calculations, such as DFT calculations.

These difficulties require more efficient routes, namely, machine learning (ML)-driven approaches [26–29]. A number of ML models aimed at predicting adsorption energies on catalytic surfaces were recently reported [30–42]. ML models including DOSnet, which requires density-of-states (DOS) as its input for adsorption energy predictions, have been developed [34,36]. Graph neural networks (GNNs), in which atoms and bonds of materials are treated as nodes and edges of graphs, outperform other models in terms of both accuracy and ease of input preparation (without DFT-level inputs) [37–40]. These GNN models were trained for diverse adsorbate types but have been used in a limited manner for exploring binary materials in both N$_2$ reduction [37] and CO$_2$ reduction catalysis [38,39]. Very recently, ML methods based on neural network potential or active learning have begun to be used to optimize the compositions for a specific ternary elemental combination [43,44]. These previous studies have highlighted the value of using ML to guide experimental material discovery [45–47]; however, exploring multicomponent systems involving at least three elements remains challenging due to both the lack of databases and ML extrapolation problems.

In this work, we present a catalyst design protocol in which ML filters out potentially efficient and low-cost electrocatalysts in the massive ternary alloy space for fuel cells. Among the many structural possibilities in the ternary space, conventional alloy core@noble metal shells ($X$$_3$$Y$@$Z$), in which all three constituent elements (X, Y and Z) can differ, are the focus of this study [48]. Based on a graph neural network trained with approximately ten thousand adsorption energy values obtained at the DFT level, we design a fully ML-driven screening process with criteria including structural stability (both thermodynamic and

mechanical), catalytic performance, and cost effectiveness. As a result, we identify 10 and 37 promising candidates for each ORR and HOR electrode, with both lower cost and higher performance than pure Pt. Through experimental verifications, we find that a Cu$_3$Au@Pt film, one of 10 final candidates for the ORR, substantially outperforms a Pt film in terms of half-wave potential, kinetic current density, and usage amount of expensive Pt. We demonstrate that our ML-based sorting protocol enables the identification of an efficient catalyst in a massive search space and could universally be expanded to other catalysis problems.

2. Experimental section

2.1. DFT database generation

Adsorption energies were calculated using the following equation: $\Delta E_{ads} = E[\text{slab} + \text{ads.}] - E[\text{slab}] - E[\text{ads.}]$, where $E[\text{slab} + \text{ads.}]$, $E[\text{slab}]$, and $E[\text{ads.}]$ indicate the DFT total energies of the slab+adsorbate, slab-only, and adsorbate-only systems, respectively. The adsorption energy was referenced to the stable and relevant gas states, including H$_2$, H$_2$O, and CO [3,49]. The Vienna Ab initio Simulation Package (VASP) was used for all DFT calculations. The projector-augmented-wave (PAW) pseudopotentials, the revised Perdew-Burke-Ernzerhof (RPBE) exchange correlation functional [50], and Grimme's DFT-D3 approach [51] (for a better description of van der Waals interactions) were used. It should be noted that the Hubbard U correction was not included in this work. Although the Hubbard U corrections are often critical for metal oxide catalyst systems with highly localized d states, they have a minor effect on the adsorption energy in pure metal systems with delocalized states (materials of current investigations) within only 0.05 eV error. A plane-wave kinetic energy cutoff of 520 eV was used. For the k-point sampling, a Monkhorst-Pack mesh of $16 \times 16 \times 16$ was used for bulk systems, and a Monkhorst-Pack mesh of $4 \times 4 \times 1$ was used for slab systems (2×2 supercells). The slabs constituted four layers, where the top two layers and adsorbates were fully relaxed until the forces acting on the individual atoms were less than 0.05 eV/Å. To avoid spurious interactions between slabs, a vacuum spacing of 15 Å (in the z-direction) was guaranteed. A total of nine adsorption sites on the (111) slabs based on the L1$_2$ alloy (M$_3$A) were considered. Fig. S1B shows these positions. First, two top sites exist: one on the matrix element (M) and the other on the alloying element (A). Next, three bridge sites exist: two between matrix-alloying elements (MA) and the other between matrix—matrix elements (MM). Finally, four hollow sites exist: two FCC sites (FCC(M) and FCC(A) classified based on the atom type at the subsurface layer) and two HCP sites (HCP(M) and HCP(A) classified likewise). The most stable sites differed by adsorbate type. Notably, H, and O species were generally stable at hollow sites rather than bridge sites. OH and CO species were placed vertically, but no particular preferences for the top, bridge, and hollow sites were observed. In the case of OOH, to minimize the substantial computational cost, we decided to limit ourselves to four adsorption sites, chosen based on their stability with respect to OH. We consistently used the various adsorption sites for each adsorbate across different materials. For each material, we considered various adsorption sites for the same adsorbate species in order to construct our database, selecting the most stable adsorption site to construct the Gibbs free energy diagram.

The free energies of the adsorbates were estimated under standard reaction conditions (pH = 0; T = 298 K; P = 1 atm) at a potential of U= 0. We assumed that the chemical potential of the solvated protons and electrons (H$^+$ + e$^-$) was in equilibrium with that of hydrogen in the gas phase (0.5 H$_2$). The thermochemical free energy was defined as $\Delta G_{ads} = \Delta E_{ads} + \Delta G_{corr}$, where ΔG_{corr} denotes the free energy correction term [37]. The reference states for the adsorbates in the ΔG_{ads} calculations were H$_2$O, H$_2$ and CO gas, as in ΔE_{ads} calculations [49,52,53]. Solvation effects were considered by employing constant values (OH: 0.5 eV, OOH: 0.25 eV) obtained from explicit water bilayer models as reported in a

previous literature [54].

2.2. ML model development

For SGCNN, the surface graph was constructed based on the crystal structures of the top two layers of the slab and adsorbates. The elemental properties of each ith atom (node) in a system were encoded into an atom vector v_i, which only constituted the information available in the periodic table of elements. For the node vector, we used the one-hot encoding method. Table S1 includes a list of atomic input features along with their ranges, units, and categories. The edge (bond between the ith and j^{th} atom) was defined only when $d_{(i,j)} < r_i + r_j + \Delta$, where $d_{(i,j)}$ denotes the distance between the ith and j^{th} atom, r_i and r_j denote the covalent radii of each atom, and Δ is the tolerance length, which was set as 1.5 Å in our work. Each bond was represented by a bond vector, $u_{(i,j)k} = 1$, where k means in the kth edge between the center node i and the neighboring node j. Note that we intentionally set the bond vector as distance-insensitive, unlike the original CGCNN work where the bond vector was divided into 10 categories. Although the bond vector treatment in CGCNN could improve the graph representation precisely, it may limit the discovery of new catalyst materials since predicting the surface properties of new materials requires information on relaxed structures. For this reason, we intentionally simplified the form of the bond vector so that the connectivity information required as an ML input was whether or not arbitrary atom pairs were connected (yes or no question) rather than distance values.

We proceeded the CNN processes on top of each surface graph, which was composed of a series of convolutions, pooling, and FCLs. The convolution functions updated each atom vector by concatenating neighbor vectors $z_{(i,j)k}^{(t,f)} = v_i^{(t,f)} \oplus v_j^{(t,f)} \oplus u_{(i,j)k}$ and then performing convolutions as follows:

$$v_i^{(t+1,f)} = v_i^{(t,f)} + \sum_{j,k} \sigma\left(z_{(i,j)k}^{(t,f)} W_1^{(t,f)} + b_1^{(t,f)}\right) \odot g(z_{(i,j)k}^{(t,f)} W_2^{(t,f)} + b_2^{(t,f)})$$

where the convolutional layer and filter numbers are denoted by the t and f parameters, respectively. $W_1^{(t,f)}$, $W_2^{(t,f)}$, and $b_1^{(t,f)}$, $b_2^{(t,f)}$ are the convolution weight matrices and biases of the tth layer and fth filter, respectively. $\oplus$ denotes concatenation, $\odot$ denotes elementwise multiplication, σ is a sigmoid function, and g is the exponential linear unit (ELU) activation function [40]. The normalized summation of all atom vectors (after R convolutions) was chosen as the pooling element, i.e., $v_{pool} = \Sigma_i{}_, f v_i^{(R,f)}$. Each atom vector was collected in the same dimension as the final function vector obtained from the pooling phase. Finally, the pooled vectors were connected with the adsorbate binding energy through the FCLs. The following hyperparameters were checked, and the optimized values are shown in parentheses: the number of convolution filters and layers (1 filter, 3 layers), learning rate (5×10^{-3}), exponentially decaying learning rate (0.97 for every 100 epochs), nodes of the FCLs (3 layers with $10 \rightarrow 4 \rightarrow 1$ nodes/layer), standard deviation of naturally distributed random initial weights (0.01), batch size (64), and total number of epochs (800). The mean squared error (MSE) was used as the loss function $J(\mathbf{y}, \mathbf{\hat{y}}(\mathbf{W}))$. The Adam optimization algorithm was used to minimize the loss function J during the training process. To minimize overfitting, we used L^2 regularization techniques. The optimized L^2 regularization coefficients were 10^{-2}. Table S2 includes a list of hyperparameters and their ranges for the optimization process.

2.3. Experimental fabrication of Cu₃Au film by sputtering

The prepared Ni electrodes were placed in a vacuum chamber of a direct-current (DC) magnetron sputtering system. To produce a Cu₃Au thin film, 99.99 % pure 3-inch Cu target and 99.99 % pure Au chips (1 cm^2) were used. Four gold chips were placed crosswise on the Cu target, two by two, and then the process was carried out. The base pressure of the vacuum chamber was 2.5×10^{-6} Torr. The working pressure was maintained at 2.5 mTorr by flowing Ar (15 sccm) gas. A DC sputtering power of 150 W was applied to the sputtering target for 30 min, leading to a Cu₃Au film 800 nm thick deposited on the substrate (for example, Ni electrodes, Si wafer).

2.4. Experimental fabrication of the Pt layer by arc plasma deposition (APD)

Pt was deposited onto the substrate (for example, Ni electrodes, Cu₃Au thin film on Ni electrode, and Si wafer) by a coaxial pulsed APD system (ULVAC, ARL-300) at room temperature under a 10^{-7} Torr vacuum. In the APD system, a cylindrical cathode composed of a Pt target and a trigger electrode were placed in the center, and a cylindrical anode was coaxially mounted to surround the cathode. A defined amount of charge was stored in a discharge capacitor connected to the cathode. When a trigger pulse induced an arc discharge between the surface of the target cathode and the anode, the accumulated charge flowed from the cathode to the anode through the arc for a short time, typically less than 1 ms. During this process, the temperature around the cathode increased by tens of thousands of degrees (°C) or more, vaporizing the cathode material and generating a high kinetic energy (>10 km s^{-1}) ionized plasma pulse. Immediately after discharging, the capacitor was rapidly recharged to generate the next plasma pulse. The controllable parameters in this process were the discharge capacitor voltage V, the discharge capacitor capacity C, and the number of plasma pulse shots **n**. In this study, V and C were set at 50 V and 1080 μF, respectively, and the deposition amount of Pt was controlled by changing **n**.

2.5. Electrochemical measurement

All electrochemical measurements were conducted with a 3-electrode rotating ring disk system using a potentiostat (Autolab, PGSTAT 302 N). A nickel disk electrode with an area of 0.196 cm^2 was used as the working electrode. Pt wire and Ag/AgCl (3 M KCl) electrodes were used as the counter and reference electrodes, respectively. The potentials vs. Ag/AgCl were converted to the reversible hydrogen electrode (RHE) using the equation below:

$$E_{RHE} = E_{Ag/AgCl} + E^{\circ}_{Ag/AgCl} + 0.0591 \text{ pH}$$

where E_{RHE} is the converted potential vs. RHE, $E^{\circ}_{Ag/AgCl} = 0.210$ at 298 K, and $E_{Ag/AgCl}$ is the experimentally measured potential against Ag/AgCl reference. The ORR curves were recorded at a scan rate of 5 mV s^{-1} with 1600 rpm in O₂-saturated 0.1 M KOH. The kinetic current density (j_k) was calculated using the Koutecky-Levich equation.

$$j_k = \frac{j_{lim} \times j}{j_{lim} - j}$$

where j is the experimentally measured current density and j_{lim} is the diffusion-limiting current density [5].

2.6. Materials characterization

The X-ray diffraction (XRD) results were measured by means of a D8-Advanced instrument (Bruker, Germany) using Cu Kα as the radiation source. Scanning electron microscopy (SEM) (Inspect F50, FEI, USA) and transmission electron microscopy (TEM) (Tecnai F20, FEI, USA) with EDS were used to examine the morphologies and structures of the samples in this study. All samples were analyzed for cross-sectional TEM images after extraction of TEM lamellae using a focused ion beam (FIB, NX5000, Hitachi, Japan).

3. Results and discussion

3.1. Adsorption energy as a fuel cell performance descriptor

The first step is to identify the descriptors for each ORR and HOR performance. For the ORR, where O_2 molecules are completely reduced to H_2O through a four-electron pathway (Fig. 1A), the rate determining step (RDS) is the largest uphill step in the free energy (ΔG) diagram along the protonation steps from O_2 to H_2O at the equilibrium potential (1.23 V vs. reversible hydrogen electrode (RHE)). Recent studies on the ORR over low-index metal surfaces suggest that one of the following two protonation steps governs the limiting potential: $O_2 + (H^+ + e^-) \rightarrow$ *OOH ($O_2 \rightarrow$ *OOH hereafter) or *OH + $(H^+ + e^-) \rightarrow H_2O$ (*OH$\rightarrow H_2O$ hereafter) [14,55]. We also confirm that the RDS is *OH$\rightarrow H_2O$ for Pt(111) and $O_2 \rightarrow$ *OOH for Au(111) (* denotes a surface site). Note that the ΔG diagrams for other metal cases are available in Fig. S2, where for some metals (Ag, Ir, Pd, and Rh) that form relatively stable *OOH intermediate states, *OH$\rightarrow H_2O$ is the RDS. Since we assume that either $O_2 \rightarrow$ *OOH or *OH$\rightarrow H_2O$ is the RDS, the limiting potential (U_L) is defined as the maximum value of $\Delta G_{*OOH} - \Delta G_{O2}$ and $\Delta G_{H2O} - \Delta G_{*OH}$ divided by the electron charge (e).

Fig. 1B shows a contour plot of the U_L values of six pure metals (with closest-packed surfaces) on the axes of ΔG_{*OOH} and ΔG_{OH}, and a quasilinear scaling relation was observed. Overcoming the scaling relation between ΔG_{*OOH} and ΔG_{*OH} is key to discovering any promising candidates with a U_L value larger than the value of 0.56 V for Pt(111), as

highlighted in the promising zone in Fig. 1B. It is well known from theories and experiments that Pt(111) shows the largest ORR U_L value of approximately 0.56 V among pure metals [56]. Thus, the U_L range of 0.56–1.23 V should be the targeted promising zone in this study.

On the other hand, the HOR is a simpler reaction (Fig. 1C), involving two proton-electron transfer reactions with only one intermediate species (*H). H_2 molecules are supplied to the anode of fuel cells, and the H_2 adsorbed on the catalytic surfaces dissociates into atomic hydrogen (*H), being finally converted to the pair of protons and electrons $(H^+ + e^-)$: $1/2\ H_2 \rightarrow$ *H $\rightarrow (H^+ + e^-)$. Herein, ΔG_{*H} serves as the HOR activity descriptor, and a $|\Delta G_{*H}|$ value smaller than 0.24 eV (that of Pt (111)) is desired. In addition, CO poisoning on the catalytic surfaces is a notorious problem for the anode; as a result, weaker CO binding is desired for fuel cell durability [56,57]. Therefore, the promising zone for the HOR is defined by the box in Fig. 1D with boundaries of $|\Delta G_{*H}|$ of 0.24 eV and ΔG_{*CO} of -1.4 eV (both values corresponding to pure Pt).

3.2. Database generation and ML model development

Previous studies in Fig. 1 confirm that the adsorption energies of five adsorbates (O, OH, OOH, H, and CO) are directly related to ORR and HOR performance. Using DFT calculations, we constructed our own surface database of 9267 adsorption energies for these five adsorbates (Fig. 2A and B). The catalytic slabs include 10 unary and 348 binary L1$_2$ alloy systems (X_3Y). For the L1$_2$ alloy, X (matrix element) is an FCC element, and Y (alloying element) is an FCC, BCC, or HCP element from
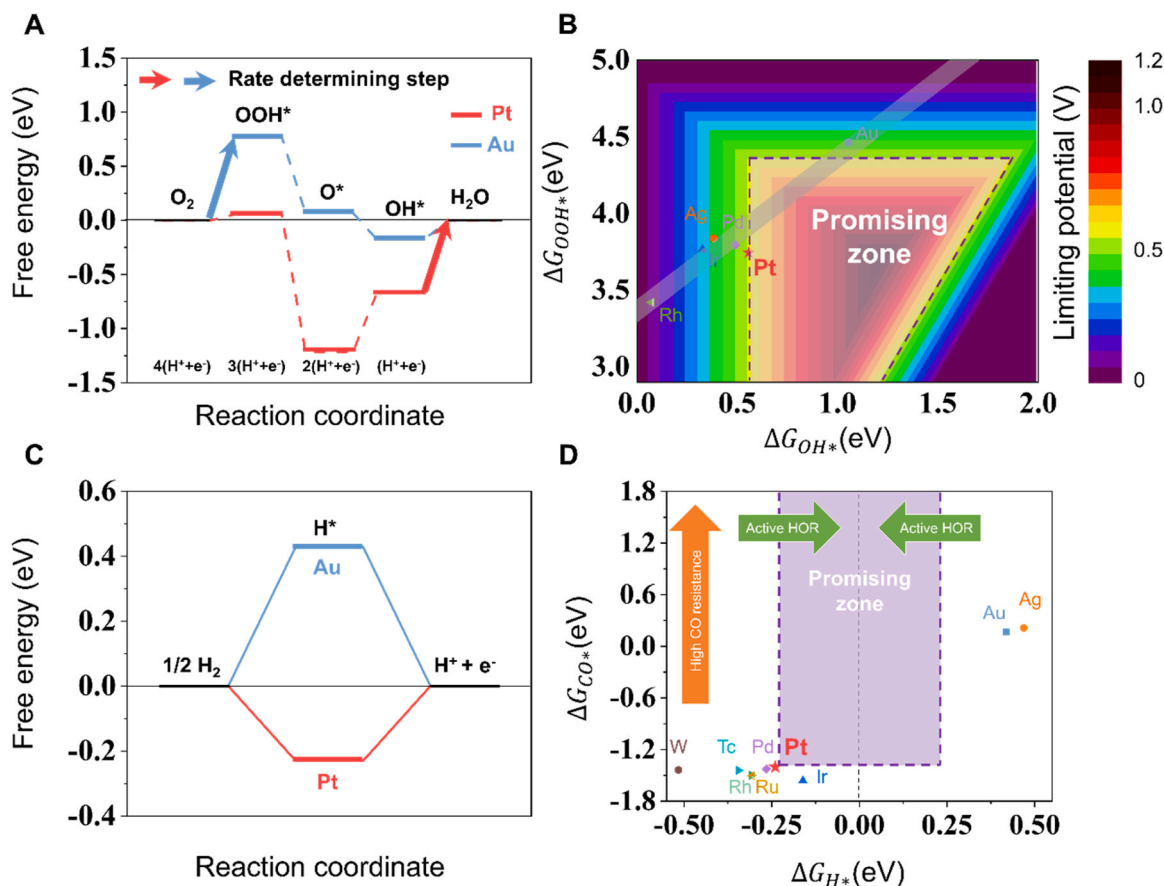

Fig. 1. Adsorption energies as ORR and HOR performance descriptors. (A) ORR Gibbs free energy diagram for associative ORR pathways on Pt(111) and Au(111). RDSs are highlighted with arrows to indicate the important step in the reaction. (B) Two-dimensional (2D) contour map of limiting potential (U_L). The six calculated pure metals are shown on the map. The contour plot highlights the scaling relation line between ΔG_{*OOH} and ΔG_{*OH} ($\Delta G_{*OOH} = \Delta G_{*OH} + 3.36$ eV), which lies in a range similar to that of a previous report[67]. The promising zone is defined as the area with a U_L value larger than 0.56 V (Pt(111) value). (C) HOR Gibbs free energy diagram of Pt(111) and Au(111). (D) Comparison of the free energies of CO and H adsorbates for 9 pure transition metals. The promising zone for the HOR is defined as the region where the $|\Delta G_{*H}|$ value is smaller than 0.24 eV and the ΔG_{*CO} value is greater than -1.4 eV (both Pt(111) values).
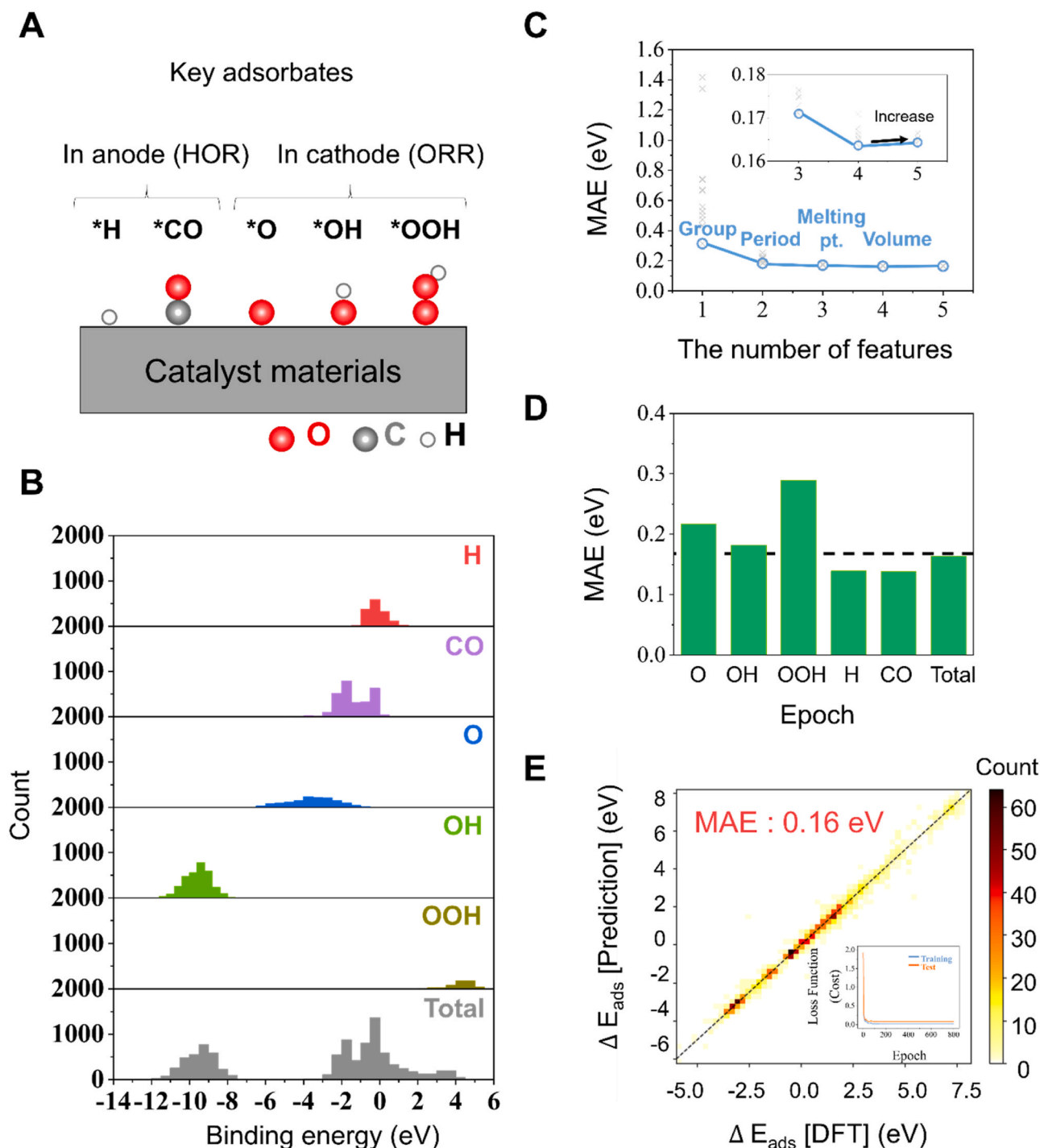
Fig. 2. Database generation and model training. (A) Types of adsorbates in the database (O, OH, OOH, H, and CO) relevant to ORR and HOR performance. (B) Adsorption energy populations for each adsorbate. This self-established database includes a total of 9267 adsorption energies for 10 unary and 348 binary L1$_2$ alloy systems ($\mathbf{X_3Y}$). The L1$_2$ alloy systems were chosen because they are composed of FCC elements (X) and FCC, BCC, and HCP elements (Y) in period numbers 2–6 and group numbers 1–14. (C) Feature optimization process of 12 types of features. The optimal combination was found to be group number, period number, melting point, and volume, leading to an MAE of 0.16 eV. (D) MAE value for each adsorbate and overall data. (E) Comparison between the predicted adsorption energy and DFT adsorption energy. The loss function change with increasing epochs is presented in the inset.

period numbers 2–6 and group numbers 1–14 on the periodic table (Fig. S1). The exposed surfaces of the slabs are (111), which is the closest-packed surface of the L1$_2$ binary alloy. More details about database generation are provided in the Methods section, and the number of data points for each adsorbate is shown in Table S3. Fig. 2B shows the population distribution of our adsorption energy (ΔE_{ads}) database for each adsorbate. Note that the energies span a very wide

range (−14 to 5 eV), and the dataset is uniformly based on various chemical elements (41 elements). Such wide and uniform data sampling is critical for the following ML developments.

The ML model to predict adsorption energy used in this work is the slab-graph convolutional neural network (SGCNN), where slab graph constructions and bond vector treatments are modified from the original CGCNN model for catalytic system applications (Fig. S3). Detailed

information about graph encoding, convolution and pooling functions, network architectures, and hyperparameters is provided in the Methods section. For node vectors, twelve elemental properties available in the periodic table of elements were considered, but the combination of only four features (group number, period number, melting point, and volume) led to the smallest error of 0.16 eV for our dataset of 9267 energy values (Fig. 2C). The addition of extra features caused overfitting and undesirably increased the mean absolute errors. In Fig. 2D and Table S4, the ML test performance of each adsorbate (O, OH, OOH, H, and CO) is shown separately. The MAE of the CO adsorbate was the smallest at 0.14 eV, probably due to the narrowest range of adsorption energies. The MAE of the OOH adsorbate was the largest at 0.29 eV, likely due to the smallest size of the corresponding dataset. The MAE value of the total dataset was 0.16 eV after 5-fold cross-validations, which is better than that in our own previous report due to the increased database size and is small enough for effective material screening processes [37]. No overfitting was observed during ML training, as shown in the inset of Fig. 2E.

3.3. A fully ML-based screening protocol

Using the well-trained ML model, we next explored the massive ternary alloy space. In this study, we focused on a particular ternary structure, namely, $L1_2$ alloy core@shell ($X_3Y@Z$) catalysts, which is not a part of our ML learning database. The harsh operating environment in fuel cells limits the shell elements (Z) in our targeted structure ($X_3Y@Z$), and we considered Pt and Au as shell elements based on the standard reduction potential. In Fig. 3, the fully ML-driven screening protocol is illustrated. This screening process was extremely fast since it did not require any DFT or equivalent theory-level inputs. For the prediction of the adsorption energy of $X_3Y@Z$ alloys, we used the same adsorption sites as with the binary alloys, with the exception of OOH. In the case of OOH, we considered top, bridge, and hollow sites without restrictions, this adjustment was facilitated by the rapid predictive capabilities of the machine learning model. A total of 3180 ternary alloys and 82,967 related slab-adsorbate structures were fed into the filtering process, which would not be practically feasible solely by using quantum
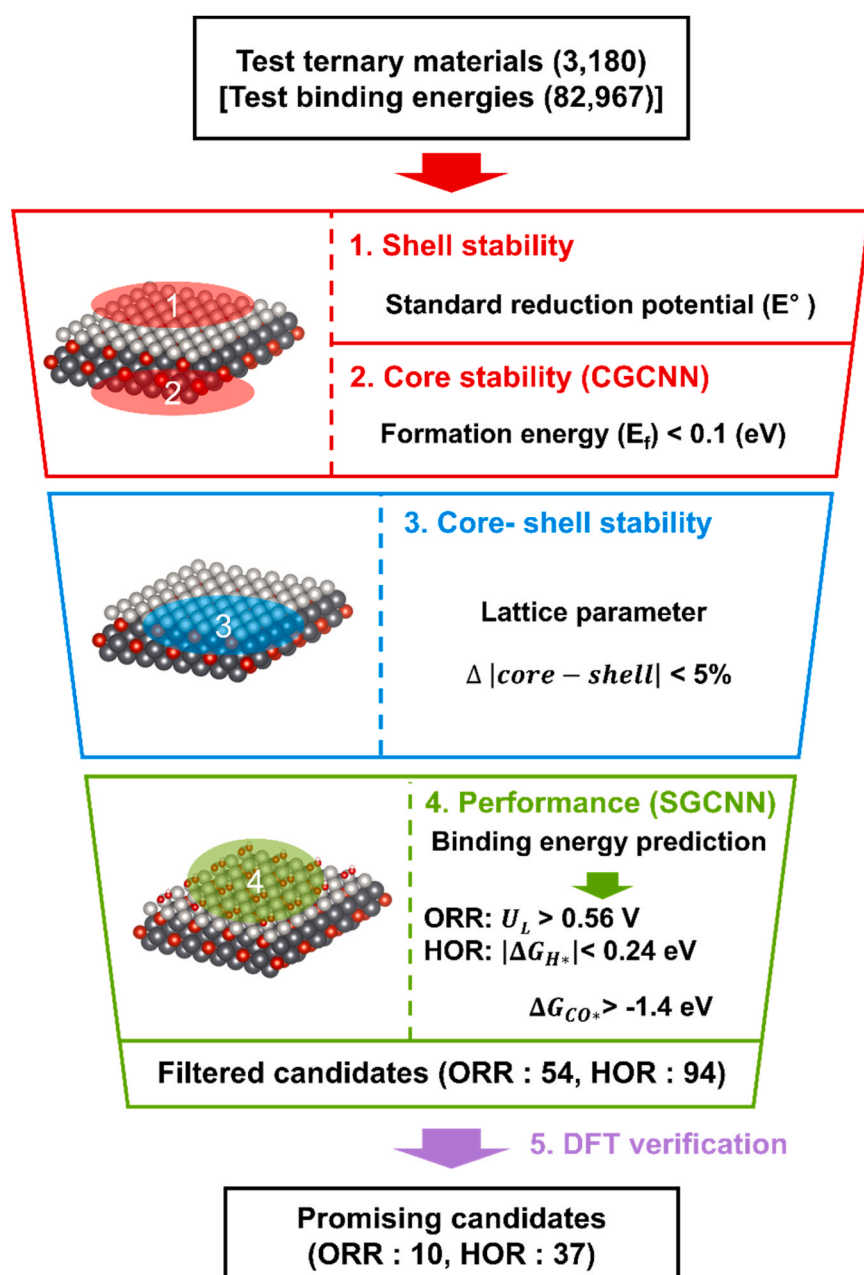

Test ternary materials (3,180)
[Test binding energies (82,967)]

1. Shell stability
Standard reduction potential (E°)

2. Core stability (CGCNN)
Formation energy (E_f) < 0.1 (eV)

3. Core- shell stability
Lattice parameter
$\Delta |core - shell| < 5\%$

4. Performance (SGCNN)
Binding energy prediction
ORR: $U_L > 0.56$ V
HOR: $|\Delta G_{H_*}| < 0.24$ eV
$\Delta G_{CO_*} > -1.4$ eV

Filtered candidates (ORR : 54, HOR : 94)

5. DFT verification

Promising candidates
(ORR : 10, HOR : 37)

Fig. 3. ML-driven material screening workflow for each anode and cathode of fuel cells. This protocol is a highly efficient and fast method for identifying promising and low-cost catalysts. The workflow involves feeding a total of 3180 ternary alloys and 82,967 related slab-adsorbate structures into a filtering process. Three criteria are used in the screening process: stability of the core and shell structures, mechanical stability between the core and shell, and catalytic performance. The stability of the shell element is determined by its electrochemical stability based on the standard reduction potential. The core stability is determined by the formation energy of the alloy core. The mechanical stability is estimated by the lattice mismatch, and the catalytic performance is predicted by the pretrained SGCNN model. Ultimately, after ML filtering and DFT verification processes, only 10 and 37 promising candidates for the ORR and HOR, respectively, survived.

mechanical calculation methods.

Three criteria were used in the screening protocols. The first is the stability of each core and shell structure. For the shell element (Z), we selected the electrochemically stable elements based on the Pourbaix diagrams that would not dissolve under the working conditions, which led to Au and Pt for the ORR and Au, Pt, Ir, Pd, Ag, Rh, Ru, Tc, Re and W for the HOR. On the other hand, for the core (X_3Y), the formation energy of each alloy core was used to estimate its thermodynamic stability (E_f <0.1 eV). We used the pretrained CGCNN model (MAE of only 0.04 eV) to predict the formation energies of these alloys. Note that the threshold here was 0.1 eV instead of zero to avoid missing any promising candidate materials.

The second screening criterion is the mechanical stability between the core and shell, which was estimated by their lattice mismatch [58]. The cases with lattice parameter mismatches larger than 5 % were not selected at this step. The last criterion is the catalytic performance, and the pretrained SGCNN model was used here. For the ORR, materials with U_L > 0.56 eV (the value of pure Pt) passed the filtering process. Similarly, for the HOR, materials with $|\Delta G_{*H}|$ < 0.24 eV and ΔG_{*CO} > −1.4 eV (the values of pure Pt) passed. In addition, we also excluded materials that included reactive elements (alkali metals and alkaline earth metals: Li, Na, K, Rb, Cs, Be, Mg, and Ba), toxic elements (Cd, Hg, Tl, and Pb), the radioactive element Tc, and the very expensive element Re. These filtering processes finally resulted in only 54 and 94 promising candidates for the ORR and HOR, respectively, which are potentially synthesizable and may outperform Pt at each electrode.

3.4. DFT verification of filtered-out candidates

Although these ML-filtered candidates are promising, they must be further examined using DFT verifications prior to experimental trials. The CGCNN and SGCNN models inevitably involve some errors in predictions for ternary materials (not a part of our training dataset), and DFT-based verifications are expected to further reduce the number of promising materials. First, for the ORR, the main checkpoint from DFT verification is whether or not U_L (limiting potential) is larger than 0.56 V (the value of pure Pt). In Fig. 4A, only 10 of the 54 ML-filtered candidates satisfied this condition even from DFT verifications, which would outperform Pt(111) for the ORR. Four of these are Au shell materials, and the remaining six are Pt shell materials, which are listed as follows in the order of high to low U_L values (DFT predictions): Pd$_3$Ta@Au (U_L=0.96 V), Pd$_3$Ti@Pt (U_L= 0.93 V), Pd$_3$V@Pt (U_L= 0.92 V), Pd$_3$Mo@Pt (U_L= 0.87 V), Pd$_3$Nb@Au (U_L=0.87 V), Cu$_3$Ti@Pt (U_L= 0.72 V), Cu$_3$Au@Pt (U_L= 0.72 V), Cu$_3$Hf@Pt (U_L= 0.72 V), Pt$_3$Mo@Au (U_L=0.71 V), and Pt$_3$Hf@Au (U_L=0.69 V). The Gibbs free energy diagrams of these materials are provided in Fig. S4. Note that these new ternary materials marked in Fig. 4A deviate from the scaling relations of unary metals, which indicates that ternary alloying indeed provides catalytic properties different from those of unary or binary cases. Interestingly, Pd$_3$V@Pt has already been reported in previous experimental work where a bimetallic alloy core was used [59]. It is noteworthy that some Au shell materials, such as Pd$_3$Ta@Au and Pd$_3$Nb@Au, show even larger U_L values than those of Pt shell materials. This result is surprising given that pure Au is only slightly active for the ORR; however, the alloy core can substantially stabilize *OOH species and modify the catalytic energetics of core@shell catalysts, as shown in Fig. S4.

In Fig. 4B, the prices of these 10 catalysts are listed. For the core@shell structure, the volume of the thin shell layer is negligibly smaller than that of the core, and thus, the price evaluations are only based on the price of the alloy core. In particular, materials with Cu as a matrix element (Cu$_3$Au@Pt, Cu$_3$Hf@Pt, and Cu$_3$Ti@Pt) are much less expensive than other candidates such as pure Pt.

In addition, the HOR candidates were also verified via DFT computations. The main checkpoint here was whether or not $|\Delta G_{*H}|$ was less than 0.24 and ΔG_{CO} was larger than − 1.4 eV to achieve high HOR
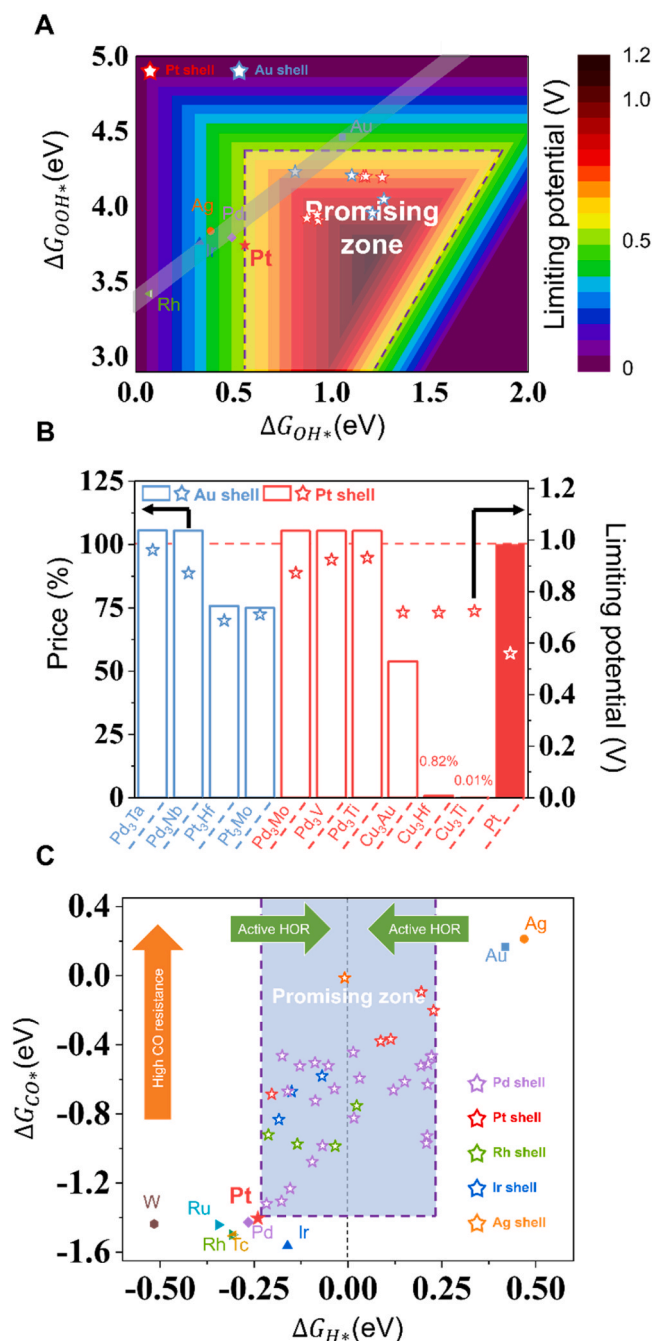

Fig. 4. DFT verification of filtered-out candidates. (A) ORR performance of the 10 promising candidates from the fully ML-driven material prediction workflow, as verified by DFT in 2D activity maps in terms of the OH and OOH free energies. Au shell and Pt shell materials are shown in blue and red, respectively. These candidates all exhibit U_L values greater than 0.56 V, which is the value of pure Pt, making them potential ORR catalysts that outperform Pt(111). (B) ORR catalytic activity (star) and material price (bar) of 10 ORR catalysts ($X_3Y@Z$). For the price axis (left axis), the platinum price is set to 100 %. Materials containing Cu as a matrix element (Cu$_3$Au@Pt, Cu$_3$Hf@Pt, and Cu$_3$Ti@Pt) are particularly cost-effective compared to other candidates and pure Pt. (C) HOR performance of the 37 promising candidates, as verified by DFT in terms of H and CO free energies. These candidates all satisfy the conditions that $|\Delta G_{*H}|$ is less than 0.24 and ΔG_{CO} is greater than − 1.4 eV.

activity and suppressed CO poisoning (for reduced CO poisoning than Pt). Only 37 materials out of 94 ML-screened candidates were selected even after the DFT verification processes as follows: 5 materials with a Pt shell, 3 materials with an Ir shell, 24 materials with a Pd shell, 1 material

with a Ag shell, and 4 materials with a Rh shell. The top five materials in terms of HOR activity are as follows in the order of high to low $|\Delta G_{*H}|$ (DFT values): Pt₃Ta@Ag ($|\Delta G_{*H}|$=0.01 eV, $\Delta G_{CO} = -0.01$ eV), Al₃Fe@Pd ($|\Delta G_{*H}|$=0.01 eV, $\Delta G_{CO} = -0.44$ eV), Al₃W@Pd ($|\Delta G_{*H}|$= 0.02 eV, $\Delta G_{CO} = -0.82$ eV), Al₃W@Rh ($|\Delta G_{*H}|$=0.02 eV, $\Delta G_{CO} = -0.76$ eV), and Al₃Co@Pd ($|\Delta G_{*H}|$=0.03 eV, $\Delta G_{CO} = -0.59$ eV). The Gibbs energy diagrams of these materials are provided in Fig. S5. Moreover, the top five candidates in terms of the CO resistance are as follows in the order of high to low ΔG_{CO} (DFT values): Pt₃Ta@Ag ($|\Delta G_{*H}|$=0.01 eV, $\Delta G_{CO} = -0.01$ eV), Al₃W@Pt ($|\Delta G_{*H}|$<0.20 eV, $\Delta G_{CO} = -0.09$ eV), Al₃Cu@Pt ($|\Delta G_{*H}|$=0.23 eV, $\Delta G_{CO} = -0.20$ eV), Al₃Au@Pt ($|\Delta G_{*H}|$=0.11 eV, $\Delta G_{CO} = -0.37$ eV), and Al₃Pd@Pt ($|\Delta G_{*H}|$=0.09 eV, $\Delta G_{CO} = -0.38$ eV). Interestingly, Pt₃Ta@Ag appeared to be the top candidate in both the $|\Delta G_{*H}|$ and ΔG_{CO} categories, potentially offering

high HOR activity and strong CO resistance. In addition, the prices of the final 37 HOR candidates are provided in Table S5. The alloy cores involving Al or Cu as the matrix element are more cost-effective than other candidates or pure Pt.

While machine learning has significantly accelerated material prediction, a substantial gap between DFT and machine learning models persists due to the still limited prediction accuracy of the latter. This discrepancy can be primarily attributed to two major factors. First, our primary target (the ternary alloys) suffer from a paucity of adsorption energy data. Considering that the goal of our research is to predict high-performing ternary alloy catalysts using a binary database, the absence of explicit incorporation of ternary alloy adsorption energy data into our analysis presents a significant challenge. Second, our machine learning model demonstrates a relatively lower predictive accuracy for OOH
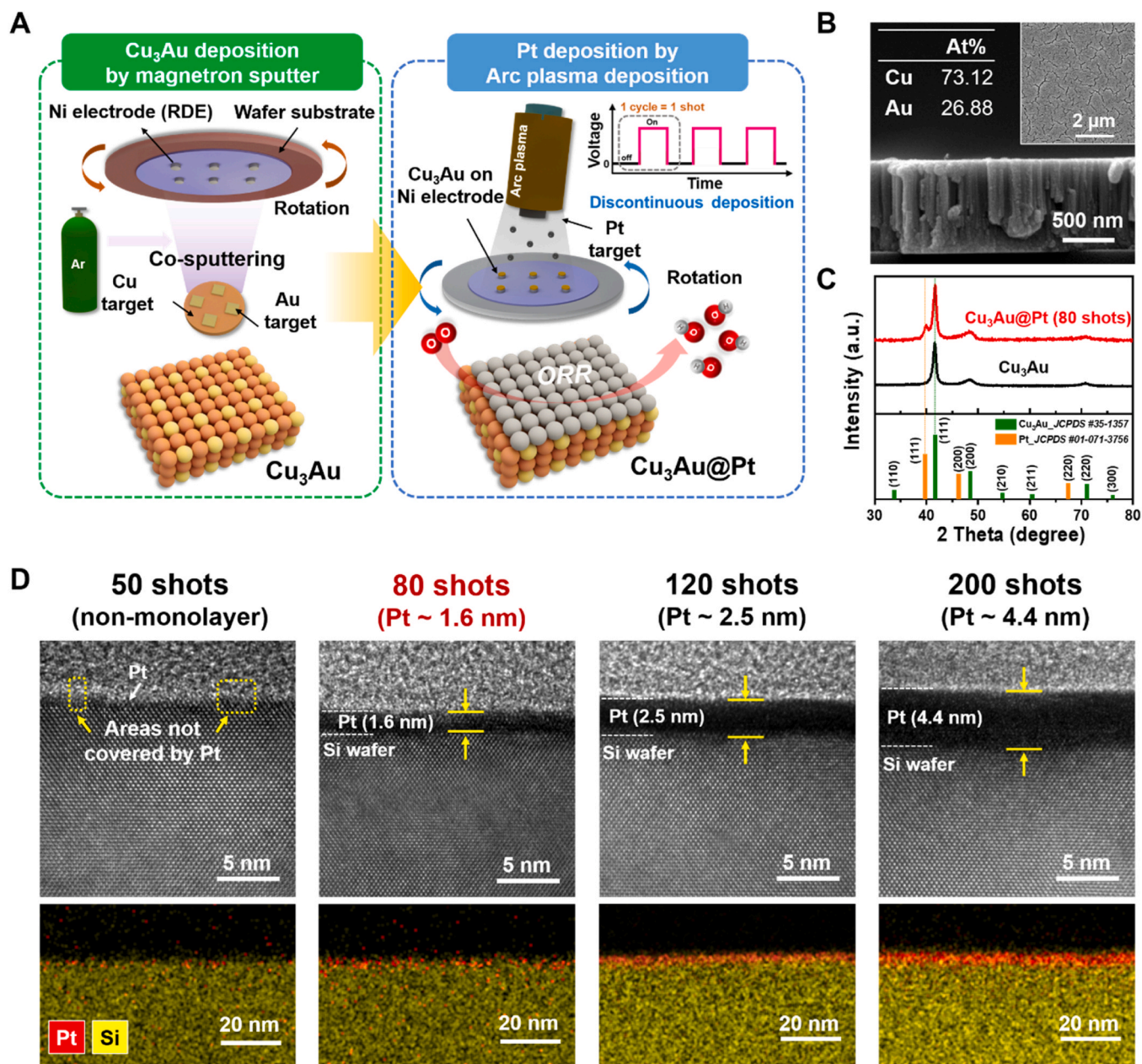

Fig. 5. Experimental fabrication and characterization of Cu₃Au@Pt thin film catalyst for ORR. (A) Schematic illustration of the fabrication process of a Cu₃Au@Pt thin film by DC-MS and APD processes. For the deposition substrate, nickel rotating disk electrodes (RDEs) were used to measure the electrochemical ORR activity, as shown in Figs. S6, S12 and S13. (B) Cross-section SEM image of Cu₃Au thin film deposited by magnetron sputtering. The insets indicate the corresponding top-view SEM image and EDS analysis result. (C) XRD spectra of pristine Cu₃Au and Cu₃Au@Pt (80 shots) thin films after Pt deposition by the APD process. (D) Cross-sectional TEM and EDS mapping images of the Pt layer depending on the number of plasma pulse shots through the APD process.

adsorbates, which contributes to the discrepancy between DFT and machine learning results. As indicated in Table S4, the predictive accuracy of our model for OOH adsorbates is lower compared to other adsorbates. This can largely be attributed to the high computational cost associated with OOH, which results in a more limited dataset for OOH adsorption energies compared to other adsorbates, as illustrated in Table S3. Moving forward, we suggest expanding the database, particularly by increasing the amount of available OOH data. We anticipate that a more comprehensive database would enable more accurate predictions, thus bridging the gap in prediction accuracy.

3.5. Experimental fabrication of novel ORR catalysts

The promising catalyst candidates suggested from the above design protocol need to be experimentally verified. Since the sluggish ORR kinetics at the cathode are the key bottleneck for fuel cell commercialization, we focused on a material for the ORR. Specifically, $Cu_3Au@Pt$. $Cu_3Au@Pt$ was chosen from the 10 candidates, primarily due to not only its higher U_L value (0.72 V) than pure Pt (0.56 V) but also its cost-effectiveness (Fig. 4B). In addition, previous experimental studies reported binary Cu_3Au alloy-based nanomaterials, supporting the potential synthesizability of the ternary $Cu_3Au@Pt$ system [60,61].

In Fig. 5A, we employed thin film fabrications rather than nanoparticles (NPs) to accurately compare the intrinsic catalytic performance between pure Pt and our ternary $Cu_3Au@Pt$ system. For core-shell NP synthesis by wet chemical processes, it is very difficult to control the shell thickness distributions of core-shell NPs [62]. Furthermore, when electrochemically testing powder-type NPs, several factors, including the catalyst ink formulation (e.g., various mixing ratios between catalyst, ionomer, and various solvents), dispersion quality and drying of the film, can substantially affect the catalytic performance, which makes accurate comparisons between pure Pt and our ternary $Cu_3Au@Pt$ systems very difficult [63,64]. Therefore, we fabricated $Cu_3Au@Pt$ thin films using dry processes based on direct-current magnetron sputtering (DC-MS) and arc plasma deposition (APD) methods so that their intrinsic catalytic properties can be evaluated by excluding those extrinsic factors.

The Cu_3Au thin film (alloy core part) was first deposited by DC-MS. The desired 3:1 stoichiometric Cu_3Au alloy was obtained by the co-sputtering process. When co-sputtering was performed on a 3-inch Cu target while increasing the number of Au chips (1 cm^2), the Au composition ratio in the formed alloy thin film gradually increased from 7.7 to 26.9 at% (Figs. S6 and S7). Through X-ray diffraction (XRD), energy dispersive spectrometry (EDS), scanning electron microscopy (SEM), and transmission electron microscopy (TEM), it was confirmed that a Cu_3Au alloy thin film (approximately 800 nm thick) was well formed (Fig. 5B, C, and Fig. S8).

The next step is Pt shell formation on top of the Cu_3Au thin films. Pt was deposited on a Cu_3Au thin film loaded in an APD chamber for precise Pt thickness control (Fig. 5A and Fig. S9). The APD technique is a type of physical vapor deposition (PVD) in which a solid metal target is directly evaporated with high-ionization plasma pulses in a vacuum environment [65]. Unlike other continuous deposition-based PVD methods such as sputtering or e-beam evaporation, APD is quite advantageous since the deposition amount can be finely tuned by the number of plasma pulse shots with a short duration (<1 ms) [66]. Precise Pt shell thickness manipulation by the APD process allows accurate analysis of alloying effects in core-shell structured catalysts. To understand Pt thicknesses depending on the number of shots (***n***), cross-sectional TEM images and the corresponding EDS mapping of the deposited Pt layer on the Si wafer are shown in Fig. 5D. The Pt thickness linearly increased as ***n*** increased (Fig. S10). As a result, for the case of 50 shots, the Pt thickness was less than 1 nm, and some regions were found that were only partially covered on the substrate (non-monolayer). For the case of 80 shots, the Pt thickness was approximately 1.6 nm, and the Pt horizontal distribution was uniform. For the others with 120 and 200

shots, the Pt films were much thicker, 2.5 nm and 4.4 nm, respectively. Additionally, we performed X-ray diffraction (XRD) measurements to investigate the interaction of Cu_3Au and Pt thin film (Fig. S11). As a result, we observed an increase in the intensity of the XRD peaks associated with Pt with increasing thickness of the Pt shell deposited on the Cu_3Au thin film and found that the peak position of the (111) crystal plane of Pt, which is typically observed at $39.75°$ in the Pt thin film, shifts to a higher angle in $Cu_3Au@Pt$ due to the compressive strain effect caused by the Cu_3Au thin film. This interaction between the Cu_3Au core and the Pt shell is responsible for the enhanced ORR properties of Pt in the core-shell compared to conventional pure Pt.

3.6. ORR performance of $Cu_3Au@Pt$

As shown in Fig. 6, the ORR characteristics of $Cu_3Au@Pt$ films with various Pt shell thicknesses on the Ni RDE electrode were investigated through the liquid half-cell. The tested samples included Cu_3Au and $Cu_3Au@Pt$ with Pt thicknesses varying from the non-monolayer to 4.4 nm. The sample with the thickest Pt film (4.4 nm) was almost identical to the pure Pt film (29.4 nm) in terms of surface ORR since the core alloying effects were negligibly small. To accurately evaluate the core-shell effects on the ORR even for very thin Pt shells in an aqueous electrolyte, the stability of the Cu_3Au core should be secured during the electrochemical measurement. For this reason, liquid half-cell tests were performed in an alkaline electrolyte (O_2-saturated 0.1 M KOH electrolyte) instead of an acidic electrolyte.

For the electrochemical measurements, the polarization curves (Fig. 6B) and Tafel plots exhibiting the kinetic current density (j_k) are presented in Fig. 6B and C, respectively. The ORR activity of $Cu_3Au@Pt$ with a 1.6 nm-thick Pt shell (80 shots in Fig. 5) was higher, with higher j_k values, than that of the other cases of the non-monolayer (50 shots), 2.5 nm (120 shots), 4.4 nm (200 shots) Pt shells, and 29.4 nm-thick Pt thin film without Cu_3Au core (1000 shots, to represent pure Pt). Interestingly, it is noteworthy that the Cu_3Au thin film without a Pt shell was also an ORR-active material, giving rise to a typical ORR polarization curve. The kinetic current density calculated at 0.85 V_{RHE} of the $Cu_3Au@Pt$ thin film (1.6 nm-thick Pt) was 1.57 mA/cm^2, which is approximately 2.2 times higher than that of the pristine Cu_3Au thin film (0.72 mA/cm^2) (Fig. 6D). This result confirms that the Cu_3Au core and Pt shell have a synergistic effect on ORR activity, in excellent agreement with our DFT and ML predictions. For the case of the non-monolayer (50 shots) Pt shell, the film's surface was not entirely covered, as shown in the TEM images (Fig. 5D), which likely led to the current density (1.09 mA/cm^2) being lower than that for the 1.6 nm case (surface fully Pt-covered). For the 2.5 nm- and 4.4 nm-thick Pt shells, the Pt shells were too thick, and the core effects were significantly diminished, leading to lower kinetic current densities of 0.91 mA/cm^2 and 0.81 mA/cm^2, respectively. The ORR activity of the 29.4 nm-thick Pt thin film was intentionally measured (Figs. S14 and S15) to represent the performance of pure Pt, and the kinetic current density was measured to be approximately 0.8 mA/cm^2. This value is almost identical to the j_k of the 4.4 nm case, indicating that the core-shell effect almost disappeared after 4.4 nm.

The catalyst with the 1.6 nm-thick Pt shell that exhibited the best ORR performance was also much more advantageous than those with thicker shells in terms of the loading amount of expensive Pt. For the 1.6 nm case, the Pt loading amount was 3.43 $μg_{Pt}/cm^2$, which is about 2.7 times and 18.4 times lower than the loading of 9.43 $μg_{Pt}/cm^2$ and 63.03 $μg_{Pt}/cm^2$ for the 4.4 nm and 29.4 nm cases, respectively. Despite the much lower Pt usage, the kinetic current density of the $Cu_3Au@$ 1.6 nm-thick Pt film was approximately two times higher than that of films with much thicker Pt thicknesses (4.4 nm and 29.4 nm) due to the core-shell effect. Since not only activity but also stability are important factors in practical application, we evaluated the electrochemical stability of $Cu_3Au@Pt$ thin film (1.6 nm-thick Pt) and 29.4 nm-thick Pt thin film in the alkaline environment for 5000 cycles of ADT
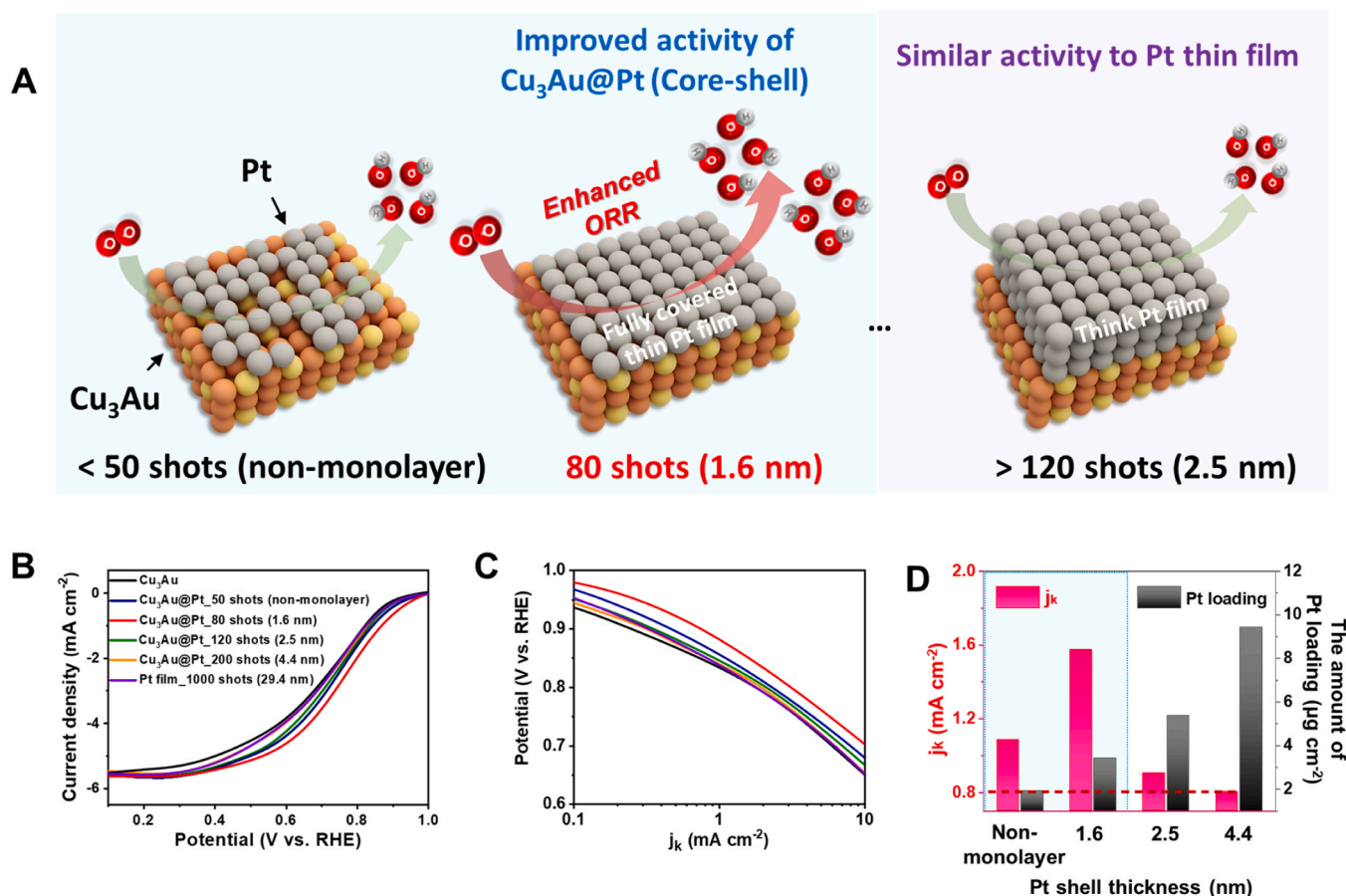
Fig. 6. Electrochemical ORR performances of Cu$_3$Au@Pt thin films. (A) Concepts of Cu$_3$Au@Pt thin film for ORR according to Pt thickness controlled by the number of plasma pulse shots in the APD process. (B) ORR polarization curves of Cu$_3$Au and Cu$_3$Au@Pt with various Pt thicknesses (non-monolayer, 1.6, 2.5 and 4.4 nm) and a Pt thin film (29.4 nm). The ORR curves were measured in an O$_2$-saturated 0.1 M KOH solution. (C) Tafel plot of the kinetic current density from polarization curves. (D) The kinetic current density at 0.85 V$_{RHE}$ and the corresponding amount of Pt loading as a function of the Pt shell thickness. The blue box in the graph indicates the region of Pt thicknesses (non-monolayer and 1.6 nm) where the core-shell effect exists. The red dashed line represents the kinetic current density of the Pt thin film (29.4 nm) without the Cu$_3$Au core thin film.

(Fig. S16). As a result, there was a slight decrease of about 7 mV for 29.4 nm-thick Pt thin film and about 9 mV for Cu$_3$Au@Pt thin film (1.6 nm-thick Pt) in terms of the half-wave potential after the ADT. In other words, the electrochemical stability of the core-shell thin films in the alkaline environment was almost comparable to that of Pt thin films, indicating that the core-shell catalysts presented in this study possess not only excellent activity but also high durability.

Additionally, we also measured the ORR performance of the Cu$_3$Au@Pt thin film (1.6 nm-thick Pt) and 29.4 nm-thick Pt thin film in an acid electrolyte (i.e., 0.1 M HClO$_4$) and found that the ORR performance of Cu$_3$Au@Pt thin film (1.6 nm-thick Pt) is much better than that of 29.4 nm-thick Pt thin film in an acidic electrolyte, likewise in an alkaline electrolyte (Fig. S17). Although a continuous decrease in ORR performance was observed during the measurement process due to the dissolution issue of the Cu$_3$Au core, the ORR performance improvement due to the core-shell effect was consistently confirmed in both acidic and alkaline environments. This result revealed that the ML-based screening and experimental verification identified both a low-cost and high-performance core-shell catalyst for fuel cells.

4. Conclusion

In summary, aiming at efficient and low-cost electrocatalysts in fuel cells, we proposed a fully ML-driven screening protocol to explore the massive ternary alloy space. A graph neural network was trained with self-established surface DFT databases to accurately predict the adsorption energy for diverse adsorbates, including H, CO, O, OH, and OOH. In our ML-based design protocol, materials were screened in terms of their structural stability, catalytic performance, and cost-effectiveness. For the ternary alloy core@shell (*X$_3$Y@Z*), this sequential process selected only 10 and 37 promising candidates for the ORR and HOR, respectively, which potentially had lower cost and higher performance than pure Pt. Finally, via experimental verifications, we observed that the film of Cu$_3$Au@Pt, one of 10 selected materials for the ORR, indeed outperformed the Pt film, as confirmed by the approximately 2-fold increase in kinetic current density with the 2.7-fold reduction in Pt usage. We demonstrated the ML-enabled identification of a fuel cell catalyst in a massive compositional space, and this protocol can be universally expanded to other multicomponent systems and catalysis problems.

Code availability

The SGCNN model is implemented using the TensorFlow framework (version 1.7.0) in Python (version 3.5). To obtain 5-fold cross-validation results for each SGCNN network using the GeForce RTX 2080 Ti GPU, approximately an hour of training time is needed. The source for the SGCNN implementation can be found in the following link: https://github.com/myungjoon/SGCNN.

CRediT authorship contribution statement

Youngtae Park: Conceptualization, Data curation, Investigation, Methodology, Project administration, and Writing – original draft. **Chang-Kyu Hwang**: Investigation, Methodology, Project administration, and Writing – original draft. **Kihoon Bang**: Validation. **Doosun Hong**: Data Curation. **Hyobin Nam**: Investigation. **Soonho Kwon**: Data curation. **Byung Chul Yeo**: Software. **Dohyun Go**: Methodology. **Jihwan An**: Investigation. **Byeong-Kwon Ju**: Investigation. **Sang Hoon Kim** : Investigation. **Ji Young Byun**: Investigation. **Seung Yong Lee**: Investigation. **Jong Min Kim**: Project administration. Supervision, and Writing – review & editing. **Donghun Kim**: Project administration, Supervision, Methodology and Writing – review & editing. **Sang Soo Han**: Project administration, Supervision, and Writing – review & editing. **Hyuck Mo Lee**: Supervision, Validation, and Writing – review & editing.

Declaration of Competing Interest

The authors declare that they have no known competing financial interests or personal relationships that could have appeared to influence the work reported in this paper.

Data Availability

Data are available from the corresponding authors on request.

Acknowledgements

Appendix A. Supporting information

Supplementary data associated with this article can be found in the online version at doi:10.1016/j.apcatb.2023.123128.

References

[1] G.W. Sievers, A.W. Jensen, J. Quinson, A. Zana, F. Bizzotto, M. Oezaslan, A. Dworzak, J.J.K. Kirkensgaard, T.E.L. Smitshuysen, S. Kadkhodazadeh, M. Juelsholt, K.M.Ø. Jensen, K. Anklam, H. Wan, J. Schäfer, K. Čépe, M. Escudero-Escribano, J. Rossmeisl, A. Quade, V. Brüser, M. Arenz, Self-supported Pt–CoO networks combining high specific activity with high surface area for oxygen reduction, Nat. Mater. 20 (2021) 208–213, https://doi.org/10.1038/s41563-020-0775-8.

[2] S. Choi, Y. Park, J. Choi, C. Lee, H.S. Cho, C.H. Kim, J. Koo, H.M. Lee, Structural effectiveness of AgCl-decorated Ag nanowires enhancing oxygen reduction, ACS Sustain. Chem. Eng. 9 (2021) 7519–7528, https://doi.org/10.1021/acssuschemeng.1c01156.

[3] J. Choi, S. Kwon, Y. Park, K. Kang, H.M. Lee, In silico high-throughput screening of Ag-based electrocatalysts for anion-exchange membrane fuel cells, J. Phys. Chem. Lett. 12 (2021) 5660–5667, https://doi.org/10.1021/acs.jpclett.1c01084.

[4] Y. Park, K. Shin, C. Lee, S.Y. Lee, Y.K. Lee, C.H. Kim, H.S. Cho, G. Henkelman, H. M. Lee, Iterative redox activation promotes interfacial synergy in an Ag/CuxO catalyst for oxygen reduction, Chem. Eng. J. 446 (2022), 136966, https://doi.org/10.1016/j.cej.2022.136966.

[5] C. Jung, C. Lee, K. Bang, J. Lim, H. Lee, H.J. Ryu, E. Cho, H.M. Lee, Synthesis of chemically ordered Pt3Fe/C intermetallic electrocatalysts for oxygen reduction reaction with enhanced activity and durability via a removable carbon coating, ACS Appl. Mater. Interfaces 9 (2017) 31806–31815, https://doi.org/10.1021/acsami.7b07648.

[6] S.M. Jung, S.W. Yun, J.H. Kim, S.H. You, J. Park, S. Lee, S.H. Chang, S.C. Chae, S. H. Joo, Y. Jung, J. Lee, J. Son, J. Snyder, V. Stamenkovic, N.M. Markovic, Y.T. Kim, Selective electrocatalysis imparted by metal–insulator transition for durability enhancement of automotive fuel cells, Nat. Catal. 3 (2020) 639–648, https://doi.org/10.1038/s41929-020-0475-4.

[7] J. Fichtner, S. Watzele, B. Garlyyev, R.M. Kluge, F. Haimerl, H.A. El-Sayed, W.J. Li, F.M. Maillard, L. Dubau, R. Chattot, J. Michaliöka, J.M. MacAk, W. Wang, D. Wang, T. Gigl, C. Hugenschmidt, A.S. Bandarenka, Tailoring the oxygen reduction activity of Pt nanoparticles through surface defects: a simple top-down approach, ACS Catal. (2020) 3131–3142, https://doi.org/10.1021/acscatal.9b04974.

[8] J.M. Kim, A. Jo, K.A. Lee, H.J. Han, Y.J. Kim, H.Y. Kim, G.R. Lee, M. Kim, Y. Park, Y.S. Kang, J. Jung, K.H. Chae, E. Lee, H.C. Ham, H. Ju, Y.S. Jung, J.Y. Kim, Conformation-modulated three-dimensional electrocatalysts for high-performance fuel cell electrodes, Sci. Adv. 7 (2021) 1–14, https://doi.org/10.1126/sciadv.abe9083.

[9] J.M. Kim, J. Kim, J. Kim, Y. Lim, Y. Kim, A. Alam, J. Lee, H. Ju, H.C. Ham, J.Y. Kim, Synergetic structural transformation of Pt electrocatalyst into advanced 3D architectures for hydrogen fuel cells, Adv. Mater. 32 (2020) 2002210, https://doi.org/10.1002/adma.202002210.

[10] L. Wang, Y. Zhou, Y. Yang, A. Subramanian, K. Kisslinger, X. Zuo, Y.C. Chuang, Y. Yin, C.Y. Nam, M.H. Rafailovich, Suppression of carbon monoxide poisoning in proton exchange membrane fuel cells via gold nanoparticle/titania ultrathin film heterogeneous catalysts, ACS Appl. Energy Mater. 2 (2019) 3479–3487, https://doi.org/10.1021/acsaem.9b00264.

[11] S.M. Zhang, K. Xiong, C.C. Jin, Z.B. Li, J.J. He, Y. Mao, Stacking fault, dislocation dissociation, and twinning in Pt3Hf compounds: a DFT study, Rare Met. 40 (2021) 1020–1030, https://doi.org/10.1007/s12598-020-01651-7.

[12] V. Stamenkovic, B.S. Mun, K.J.J. Mayrhofer, P.N. Ross, N.M. Markovic, J. Rossmeisl, J. Greeley, J.K. Nørskov, Changing the activity of electrocatalysts for oxygen reduction by tuning the surface electronic structure, Angew. Chem. - Int. Ed. 45 (2006) 2897–2901, https://doi.org/10.1002/anie.200504386.

[13] V.R. Stamenkovic, B. Fowler, B.S. Mun, G. Wang, P.N. Ross, C.A. Lucas, N. M. Marković, Improved oxygen reduction activity on Pt 3 Ni(111) via increased surface site availability, in: Science, 315, 2007, pp. 493–497, https://doi.org/10.1126/science.1135941.

[14] J. Greeley, I.E.L. Stephens, A.S. Bondarenko, T.P. Johansson, H.A. Hansen, T. F. Jaramillo, J. Rossmeisl, I. Chorkendorff, J.K. Nørskov, Alloys of platinum and early transition metals as oxygen reduction electrocatalysts, Nat. Chem. 1 (2009) 552–556, https://doi.org/10.1038/nchem.367.

[15] K. Jiang, D. Zhao, S. Guo, X. Zhang, X. Zhu, J. Guo, G. Lu, X. Huang, Efficient oxygen reduction catalysis by subnanometer Pt alloy nanowires, Sci. Adv. 3 (2017) 2–10, https://doi.org/10.1126/sciadv.1601705.

[16] L. Bu, S. Guo, X. Zhang, X. Shen, D. Su, G. Lu, X. Zhu, J. Yao, J. Guo, X. Huang, Surface engineering of hierarchical platinum-cobalt nanowires for efficient electrocatalysis, Nat. Commun. 7 (2016) 11850, https://doi.org/10.1038/ncomms11850.

[17] L. Chong, J. Wen, J. Kubal, F.G. Sen, J. Zou, J. Greeley, M. Chan, H. Barkholtz, W. Ding, D.J. Liu, Ultralow-loading platinum-cobalt fuel cell catalysts derived from imidazolate frameworks, Science 362 (80) (2018) 1276–1281, https://doi.org/10.1126/science.aau0630.

[18] J. Kang, S.H. Noh, J. Hwang, H. Chun, H. Kim, B. Han, First-principles database driven computational neural network approach to the discovery of active ternary nanocatalysts for oxygen reduction reaction, Phys. Chem. Chem. Phys. 20 (2018) 24539–24544, https://doi.org/10.1039/c8cp03801e.

[19] X. Tan, S. Prabhudev, A. Kohandehghan, D. Karpuzov, G.A. Botton, D. Mitlin, Pt-Au-Co alloy electrocatalysts demonstrating enhanced activity and durability toward the oxygen reduction reaction, ACS Catal. 5 (2015) 1513–1524, https://doi.org/10.1021/cs501710b.

[20] C. Zhang, W. Sandorf, Z. Peng, Octahedral Pt2CuNi uniform alloy nanoparticle catalyst with high activity and promising stability for oxygen reduction reaction, ACS Catal. 5 (2015) 2296–2300, https://doi.org/10.1021/cs502112g.

[21] S.J. Hwang, S.J. Yoo, S. Jang, T.H. Lim, S.A. Hong, S.K. Kim, Ternary Pt-Fe-Co alloy electrocatalysts prepared by electrodeposition: elucidating the roles of Fe and co in the oxygen reduction reaction, J. Phys. Chem. C 115 (2011) 2483–2488, https://doi.org/10.1021/jp106947q.

[22] C. Wang, D. Li, M. Chi, J. Pearson, R.B. Rankin, J. Greeley, Z. Duan, G. Wang, D. Van Der Vliet, K.L. More, N.M. Markovic, V.R. Stamenkovic, Rational development of ternary alloy electrocatalysts, J. Phys. Chem. Lett. 3 (2012) 1668–1673, https://doi.org/10.1021/jz300563z.

[23] J. Li, H.-M. Yin, X.-B. Li, E. Okunishi, Y.-L. Shen, J. He, Z.-K. Tang, W.-X. Wang, E. Yücelen, C. Li, Y. Gong, L. Gu, S. Miao, L.-M. Liu, J. Luo, Y. Ding, Surface evolution of a Pt–Pd–Au electrocatalyst for stable oxygen reduction, Nat. Energy 2 (2017) 17111, https://doi.org/10.1038/nenergy.2017.111.

[24] R.M. Arán-Ais, F. Dionigi, T. Merzdorf, M. Gocyla, M. Heggen, R.E. Dunin-Borkowski, M. Gliech, J. Solla-Gullón, E. Herrero, J.M. Feliu, P. Strasser, Elemental anisotropic growth and atomic-scale structure of shape-controlled octahedral Pt–Ni–Co alloy nanocatalysts, Nano Lett. 15 (2015) 7473–7480, https://doi.org/10.1021/acs.nanolett.5b03057.

[25] J. Huang, L. Sementa, Z. Liu, G. Barcaro, M. Feng, E. Liu, L. Jiao, M. Xu, D. Leshchev, S.-J. Lee, M. Li, C. Wan, E. Zhu, Y. Liu, B. Peng, X. Duan, W. A. Goddard, A. Fortunelli, Q. Jia, Y. Huang, Experimental Sabatier plot for predictive design of active and stable Pt-alloy oxygen reduction reaction catalysts, Nat. Catal. 5 (2022) 513–523, https://doi.org/10.1038/s41929-022-00797-0.

[26] D. Hong, J. Oh, K. Bang, S. Kwon, S. Yun, H.M. Lee, Interpretable deep learning model for analyzing the relationship between the electronic structure and chemisorption property, J. Phys. Chem. Lett. (2022) 8628–8634, https://doi.org/10.1021/acs.jpclett.2c02293.

[27] K. Bang, B.C. Yeo, D. Kim, S.S. Han, H.M. Lee, Accelerated mapping of electronic density of states patterns of metallic nanoparticles via machine-learning, Sci. Rep. 11 (2021) 1–11, https://doi.org/10.1038/s41598-021-91068-8.

[28] S. Kapse, S. Janwari, U.V. Waghmare, R. Thapa, Energy parameter and electronic descriptor for carbon based catalyst predicted using QM/ML, Appl. Catal. B Environ. 286 (2021), 119866, https://doi.org/10.1016/j.apcatb.2020.119866.

[29] S.R. Denny, Z. Lin, W.N. Porter, N. Artrith, J.G. Chen, Machine learning prediction and experimental verification of Pt-modified nitride catalysts for ethanol reforming with reduced precious metal loading, Appl. Catal. B Environ. 312 (2022), 121380, https://doi.org/10.1016/j.apcatb.2022.121380.

[30] Z. Li, S. Wang, W.S. Chin, L.E. Achenie, H. Xin, High-throughput screening of bimetallic catalysts enabled by machine learning, J. Mater. Chem. A 5 (2017) 24131–24138, https://doi.org/10.1039/c7ta01812f.

[31] M. Sun, A.W. Dougherty, B. Huang, Y. Li, C. Yan, Accelerating atomic catalyst discovery by theoretical calculations-machine learning strategy, Adv. Energy Mater. 10 (2020) 1903949, https://doi.org/10.1002/aenm.201903949.

[32] X. Ma, Z. Li, L.E.K. Achenie, H. Xin, Machine-learning-augmented chemisorption model for CO_2 electroreduction catalyst screening, J. Phys. Chem. Lett. 6 (2015) 3528–3533, https://doi.org/10.1021/acs.jpclett.5b01660.

[33] T. Toyao, K. Suzuki, S. Kikuchi, S. Takakusagi, K.I. Shimizu, I. Takigawa, Toward effective utilization of methane: machine learning prediction of adsorption energies on metal alloys, J. Phys. Chem. C. 122 (2018) 8315–8326, https://doi.org/10.1021/acs.jpcc.7b12670.

[34] X. Li, R. Chiong, A.J. Page, Group and period-based representations for improved machine learning prediction of heterogeneous alloy catalysts, J. Phys. Chem. Lett. 12 (2021) 5156–5162, https://doi.org/10.1021/acs.jpclett.1c01319.

[35] R. Gasper, H. Shi, A. Ramasubramaniam, Adsorption of CO on low-energy, low-symmetry Pt nanoparticles: energy decomposition analysis and prediction via machine-learning models, J. Phys. Chem. C. 121 (2017) 5612–5619, https://doi.org/10.1021/acs.jpcc.6b12800.

[36] V. Fung, G. Hu, P. Ganesh, B.G. Sumpter, Machine learned features from density of states for accurate adsorption energy prediction, Nat. Commun. 12 (2021), https://doi.org/10.1038/s41467-020-20342-6.

[37] M. Kim, B.C. Yeo, Y. Park, H.M. Lee, S.S. Han, D. Kim, Artificial intelligence to accelerate the discovery of N2 electroreduction catalysts, Chem. Mater. 32 (2020) 709–720, https://doi.org/10.1021/acs.chemmater.9b03686.

[38] G.H. Gu, J. Noh, S. Kim, S. Back, Z. Ulissi, Y. Jung, Practical deep-learning representation for fast heterogeneous catalyst screening, J. Phys. Chem. Lett. 11 (2020) 3185–3191, https://doi.org/10.1021/acs.jpclett.0c00634.

[39] S. Back, J. Yoon, N. Tian, W. Zhong, K. Tran, Z.W. Ulissi, Convolutional neural network of atomic surface structures to predict binding energies for high-throughput screening of catalysts, J. Phys. Chem. Lett. 10 (2019) 4401–4408, https://doi.org/10.1021/acs.jpclett.9b01428.

[40] T. Xie, J.C. Grossman, Crystal graph convolutional neural networks for an accurate and interpretable prediction of material properties, Phys. Rev. Lett. 120 (2018), 145301, https://doi.org/10.1103/PhysRevLett.120.145301.

[41] K. Tran, Z.W. Ulissi, Active learning across intermetallics to guide discovery of electrocatalysts for CO_2 reduction and H2 evolution, Nat. Catal. 1 (2018) 696–703, https://doi.org/10.1038/s41929-018-0142-1.

[42] M. Zhong, K. Tran, Y. Min, C. Wang, Z. Wang, C.T. Dinh, P. De Luna, Z. Yu, A. S. Rasouli, P. Brodersen, S. Sun, O. Voznyy, C.S. Tan, M. Askerka, F. Che, M. Liu, A. Seifitokaldani, Y. Pang, S.C. Lo, A. Ip, Z. Ulissi, E.H. Sargent, Accelerated discovery of CO_2 electrocatalysts using active machine learning, Nature 581 (2020) 178–183, https://doi.org/10.1038/s41586-020-2242-8.

[43] M. Kim, M.Y. Ha, W. Jung, J. Yoon, E. Shin, I. Kim, W.B. Lee, Y. Kim, H. Jung, Searching for an optimal multi-metallic alloy catalyst by active learning combined with experiments, Adv. Mater. 34 (2022) 2108900, https://doi.org/10.1002/adma.202108900.

[44] H. Chun, E. Lee, K. Nam, J.-H. Jang, W. Kyoung, S.H. Noh, B. Han, First-principle-data-integrated machine-learning approach for high-throughput searching of ternary electrocatalyst toward oxygen reduction reaction, Chem. Catal. 1 (2021) 855–869, https://doi.org/10.1016/j.checat.2021.06.001.

[45] A. Smith, A. Keane, J.A. Dumesic, G.W. Huber, V.M. Zavala, A machine learning framework for the analysis and prediction of catalytic activity from experimental data, Appl. Catal. B Environ. 263 (2020) 118257, https://doi.org/10.1016/j.apcatb.2019.118257.

[46] M. Suvarna, T.P. Araújo, J. Pérez-Ramírez, A generalized machine learning framework to predict the space-time yield of methanol from thermocatalytic CO_2 hydrogenation, Appl. Catal. B Environ. 315 (2022), https://doi.org/10.1016/j.apcatb.2022.121530.

[47] K. Broderick, E. Lopato, B. Wander, S. Bernhard, J. Kitchin, Z. Ulissi, Identifying limitations in screening high-throughput photocatalytic bimetallic nanoparticles with machine-learned hydrogen adsorptions, Appl. Catal. B Environ. 320 (2023), 121959, https://doi.org/10.1016/j.apcatb.2022.121959.

[48] L. Zhang, G. Henkelman, Computational design of alloy-core@shell metal nanoparticle catalysts, ACS Catal. 5 (2015) 655–660, https://doi.org/10.1021/cs501176b.

[49] I.C. Man, H.Y. Su, F. Calle-Vallejo, H.A. Hansen, J.I. Martínez, N.G. Inoglu, J. Kitchin, T.F. Jaramillo, J.K. Nørskov, J. Rossmeisl, Universality in oxygen evolution electrocatalysis on oxide surfaces, ChemCatChem 3 (2011) 1159–1165, https://doi.org/10.1002/cctc.201000397.

[50] B. Hammer, L.B. Hansen, J.K. Nørskov, Improved adsorption energetics within density-functional theory using revised Perdew-Burke-Ernzerhof functionals, Phys. Rev. B - Condens. Matter Mater. 59 (1999) 7413–7421, https://doi.org/10.1103/PhysRevB.59.7413.

[51] J. Moellmann, S. Grimme, DFT-D3 study of some molecular crystals, J. Phys. Chem. C. 118 (2014) 7615–7621, https://doi.org/10.1021/jp501237c.

[52] J.K. Nørskov, J. Rossmeisl, A. Logadottir, L. Lindqvist, J.R. Kitchin, T. Bligaard, H. Jónsson, Origin of the overpotential for oxygen reduction at a fuel-cell cathode, J. Phys. Chem. B 108 (2004) 17886–17892, https://doi.org/10.1021/jp047349j.

[53] S. Back, J. Na, K. Tran, Z.W. Ulissi, In silicodiscovery of active, stable, CO-tolerant and cost-effective electrocatalysts for hydrogen evolution and oxidation, Phys. Chem. Chem. Phys. 22 (2020) 19454–19458, https://doi.org/10.1039/d0cp03017a.

[54] Q. Zhang, A. Asthagiri, Solvation effects on DFT predictions of ORR activity on metal surfaces, Catal. Today 323 (2019) 35–43, https://doi.org/10.1016/j.cattod.2018.07.036.

[55] H.A. Hansen, J. Rossmeisl, J.K. Nørskov, Surface Pourbaix diagrams and oxygen reduction activity of Pt, Ag and Ni(111) surfaces studied by DFT, Phys. Chem. Chem. Phys. 10 (2008) 3722–3730, https://doi.org/10.1039/b803956a.

[56] O.T. Holton, J.W. Stevenson, The role of platinum in proton exchange membrane fuel cells, Platin. Met. Rev. 57 (2013) 259–271, https://doi.org/10.1595/147106713×671222.

[57] J. Min, A.A. Jeffery, Y. Kim, N. Jung, Electrochemical analysis for demonstrating CO tolerance of catalysts in polymer electrolyte membrane fuel cells, Nanomaterials 9 (2019), https://doi.org/10.3390/nano9101425.

[58] J.J. Fang, Q.M. Liu, X.W. Kang, S.W. Chen, Selective hydrogenation of 4-nitro-styrene to 4-nitroethylbenzene catalyzed by Pd@Ru core–shell nanocubes, Rare Met. 41 (2022) 1189–1194, https://doi.org/10.1007/s12598-021-01868-0.

[59] S. Liu, L. Han, J. Zhu, W. Xiao, J. Wang, H. Liu, H. Xin, D. Wang, Enhanced electrocatalytic activity and stability of Pd3V/C nanoparticles with a trace amount of Pt decoration for the oxygen reduction reaction, J. Mater. Chem. A 3 (2015) 20966–20972, https://doi.org/10.1039/c5ta05202e.

[60] A.K. Sra, T.D. Ewers, R.E. Schaak, Direct solution synthesis of intermetallic AuCu and AuCu3 nanocrystals and nanowire networks, Chem. Mater. 17 (2005) 758–766, https://doi.org/10.1021/cm0484450.

[61] Z. Niu, S. Chen, Y. Yu, T. Lei, A. Dehestani, K. Schierle-Arndt, P. Yang, Morphology-controlled transformation of Cu@Au core-shell nanowires into thermally stable Cu3Au intermetallic nanowires, Nano Res 13 (2020) 2564–2569, https://doi.org/10.1007/s12274-020-2900-z.

[62] J. Kim, Y. Hong, K. Lee, J.Y. Kim, Highly stable Pt-based ternary systems for oxygen reduction reaction in acidic electrolytes, Adv. Energy Mater. 10 (2020) 2002049, https://doi.org/10.1002/aenm.202002049.

[63] Y. Garsany, J. Ge, J. St-Pierre, R. Rocheleau, K.E. Swider-Lyons, Analytical procedure for accurate comparison of rotating disk electrode results for the oxygen reduction activity of Pt/C, J. Electrochem. Soc. 161 (2014) F628–F640, https://doi.org/10.1149/2.036405jes.

[64] Y. Garsany, J. Ge, J. St-Pierre, R. Rocheleau, K. Swider-Lyons, Standardizing thin-film rotating disk electrode measurements of the oxygen reduction activity of Pt/C, 1238–1238, ECS Meet. Abstr. MA2013-02 (2013), https://doi.org/10.1149/MA2013-02/15/1238.

[65] S.H. Kim, Y.E. Jeong, H. Ha, J.Y. Byun, Y.D. Kim, Ultra-small platinum and gold nanoparticles by arc plasma deposition, Appl. Surf. Sci. 297 (2014) 52–58, https://doi.org/10.1016/j.apsusc.2014.01.072.

[66] S.H. Kim, S.-Y. Moon, J.Y. Park, Non-colloidal nanocatalysts fabricated using Arc plasma deposition and their application in heterogenous catalysis and photocatalysis, Top. Catal. 60 (2017) 812–822, https://doi.org/10.1007/s11244-017-0746-8.

[67] S. Deshpande, J.R. Kitchin, V. Viswanathan, Quantifying uncertainty in activity volcano relationships for oxygen reduction reaction, ACS Catal. 6 (2016) 5251–5259, https://doi.org/10.1021/acscatal.6b00509.